JBC Papers in Press. Published on November 6, 2020 as Manuscript RA120.016019
The latest version is at https://www.jbc.org/cgi/doi/10.1074/jbc.RA120.016019

Structural basis of carnitine monooxygenase CntA substrate specificity, inhibition and inter-subunit electron transfer

Mussa Quareshy[1], Muralidharan Shanmugam[2], Eleanor Townsend[1], Eleanor Jameson[1], Timothy D.H. Bugg[3], Alexander D. Cameron[1], Yin Chen[1]

[1] School of Life Sciences, University of Warwick, Gibbet Hill Road, Coventry, CV4 7AL, U.K.

[2] Manchester Institute of Biotechnology, The University of Manchester, 131 Princess Street, Manchester, M1 7DN, U.K.

[3] Department of Chemistry, University of Warwick, Gibbet Hill Road, Coventry, CV4 7AL, U.K.

Correspondence to Dr. M Quareshy (mussaquareshy@gmail.com) or Prof. Y Chen (y.chen.25@warwick.ac.uk, 00442476528976)

Running title: structure and inhibition of CntA

Keywords: gut microbiota, carnitine oxygenase, CntA, EPR, inhibitor

Abstract
Microbial metabolism of carnitine to trimethylamine (TMA) in the gut can accelerate atherosclerosis and heart disease and these TMA-producing enzymes are therefore important drug targets. Here, we report the first structures of the carnitine oxygenase CntA, an enzyme of the Rieske oxygenase family. CntA exists in a head-to-tail α_3 trimeric structure. The two functional domains (the Rieske and the catalytic mononuclear iron domains) are located > 40 Å apart in the same monomer but adjacent in two neighbouring monomers. Structural determination of CntA and subsequent electron paramagnetic resonance measurements uncover the molecular basis of the so-called bridging glutamate (E205) residue in inter-subunit electron transfer. The structures of the substrate-bound CntA help to define the substrate pocket. Importantly, a tyrosine residue (Y203) is essential for ligand recognition through a π-cation interaction with the quaternary ammonium group. This interaction between an aromatic residue and quaternary amine substrates allows us to delineate a subgroup of Rieske oxygenases (group V) from the prototype ring-hydroxylating Rieske oxygenases involved in bioremediation of aromatic pollutants in the environment. Furthermore, we report the discovery of the first known CntA inhibitors and solve the structure of CntA in complex with the inhibitor, demonstrating the pivotal role of Y203 through a π-π stacking interaction with the inhibitor. Our study provides the structural and molecular basis for future discovery of drugs targeting this TMA-producing enzyme in human gut.

Introduction

The vast array of co-habiting microorganisms in the human gut impose a discernible influence on human wellbeing and disease states. There is a considerable interest in the past decade to investigate the formation of methylated amines in human health, particularly with regard to cardiovascular diseases and non-alcoholic fatty liver diseases (1-5). Dietary intake of quaternary amines such as choline and carnitine, both of which are prevalent in the human diet, can be processed by gut microbiota to produce small methylated amines (*e.g.* trimethylamine, TMA), which enter vascular circulation leading to subsequent hepatic oxidation to trimethylamine oxide (TMAO). TMAO is linked to cardiovascular disease, kidney disease, diabetes and various forms of cancers (6-8). These TMA-producing and metabolising enzymes from gut microbiota therefore represent promising new drug targets (9-11).

The key microbial enzymes responsible for TMA formation from choline and carnitine have only been identified relatively recently (12-14). Choline-TMA lyases belong to a large family of proteins, attacking the carbon-nitrogen (C-N) bond in choline using a radical species generated from a conserved glycine residue. The structure of choline-TMA lyase CutC has been solved recently (16-17), aiding the development of inhibitors (substrate analogues) for attenuating TMA formation from choline (18-21). The carnitine monooxygenase (CntA) and associated reductase (CntB) responsible for carnitine oxidation to TMA (Figure 1A) was originally identified in *Acinetobacter* spp. but was subsequently found to be present in a range of gut microbiota species (13-15). CntA belongs to a large group of non-heme iron-containing Rieske oxygenase family (13). Rieske oxygenases are typically multicomponent enzyme systems involving an oxygenase, a reductase and sometimes a separate flavin cofactor (22). The oxygenase component has a

conserved [2Fe-2S] Rieske centre coordinated by two cysteine and two histidine residues and a catalytic mononuclear iron (Fe) centre (23-24). A reductase component reduces pyridine nucleotides, generating electrons which are ultimately transferred to the Rieske oxygenase for substrate oxidation. The archetypal Rieske oxygenases, also known as ring-hydroxylating Rieske oxygenases, catalyse the oxidation of a range of aromatic and polyaromatic substrates; as such, they are important in bioremediation of environmental pollutants (24-25). Structural determination of several ring-hydroxylating Rieske oxygenases (*e.g*. naphthalene dioxygenase and biphenyl dioxygenase) reveals that the Rieske centre and the catalytic mononuclear Fe centre are usually far apart in the same subunit (>40 Å) and effective electron transfer can only occur across the interface of two neighbouring subunits (23, 26, 27).

It has becoming increasingly clear that quaternary amines-oxidising Rieske oxygenases represent a new emerging clade of the Rieske oxygenases family that is distinct from the archetypal ring-hydroxylating aromatic Rieske oxygenases (13, 27-29). The carnitine-degrading CntA enzyme is a promising new drug target, given that gut microbial metabolism of carnitine is known to increase plasma TMAO, leading to the subsequent development of atherosclerosis and cardiovascular diseases (9). However, no structure of CntA or description of possible inhibitors have been published. In this study, we report high-resolution crystal structures of CntA with and without substrates-bound and report the first known inhibitors for this enzyme and the crystal structure of an inhibitor-bound CntA. Structure, biochemical and electron paramagnetic resonance (EPR) characterisation CntA and mutants provides novel insights into the mode of inhibition and the inter-/intra- subunit electron transfer in carnitine oxidation. Our work therefore provides the structural and molecular basis for future discovery of drugs targeting this TMA-producing enzyme in human gut.

Results

Structure determination of CntA

We set out to solve the structure of CntA from *A. baumannii* and we successfully obtained structures of CntA in the apo protein form (2.1 Å, PDB 6Y8J) and ligand-bound forms with two substrates, carnitine (2.0 Å, PDB 6Y9D) and γ-butyrobetaine ((gBB), 1.6 Å, PDB 6Y8S) (Table 1). We observed a head-to-tail α_3 trimeric structure for CntA (Figure 1B), with the Rieske [2Fe-2S] cluster and mononuclear Fe centre at opposing regions of the monomer 44 Å apart (Figure 1C). The observed assembly of α_3 homotrimer is in agreement with the analyses by native protein gel (13) and analytic gel filtration (*Figure S1*). The two CntA substrate bound structures and apo form are superimposable with an average root-mean-square deviation (rmsd) of 0.487 Å (*Table S1*).

For all three structures, the Rieske [2Fe-2S] cluster is well-defined and coordinated by two histidine and two cysteine residues (Figure 1D, *Figure S2A*). This Rieske centre is structurally conserved in all Rieske oxygenases, such as stachydrine demethylase Stc2 (28), naphthalene 1,2-dioxygenase NdoB (26) and dicamba monooxygenase DdmC (30) (*Figure S2B*). The active sites containing mononuclear Fe centres are, however, considerably varied in enzymes of the Rieske oxygenase family (*Figure S2B*), reflecting the diverse catalytic reactions catalysed by these enzymes. The mononuclear Fe exists in an octahedral geometry and is coordinated by two

histidine ligands (His 213, His 208) and a bidentate aspartate residue (Asp 323) in a well-documented His-His-Asp catalytic triad (31), co-ordinating one face of the Fe centre (Figure 1E). A pair of reduced Cys (Cys206, Cys209) is found near the mononuclear Fe in CntA whereas in stachydrine demethylase Stc2 the corresponding Cys formed a disulphide bridge (28). A water molecule and a thiocyanate $[SCN]^-$ anion occupy the two co-ordination sites, which are 2.2 Å and 2.3 Å away from the mononuclear Fe centre in CntA, respectively (Figure 1E, *Figure S2C*). Both the water molecule and $[SCN]^-$ are positioned 3.7 Å below the Cα adjacent to the carnitine ammonium group, which is expected to be the site of hydroxylation catalysed by this enzyme (Figure 1E). SCN- bound at the O_2 site likely resulted in the stabilisation of CntA co-crystalized with the substrates. The catalytic mononuclear Fe in purified CntA is in a ferrous (Fe^{2+}) state, showing no EPR signals associated with either high-spin (S = 5/2) or low-spin (S = ½) ferric centre (Fe^{3+}) despite purifying the protein under aerobic conditions. This is confirmed by the addition of nitric oxide (NO) to CntA, showing an EPR signal from a S = ½ species of the Fe^{2+}-NO adduct (Figure 1F). This is contrast to the other non-heme oxygenase enzymes, where NO binding to the mononuclear iron centre often led to the formation of high-spin, S = 3/2 signal (32). This plausibly suggests that the mononuclear iron ion exists as an S = 0 in its ferrous state. The observed EPR signal for the Fe^{2+}-NO adduct is similar to the previously reported heme/non-heme-NO adducts (33-34).

Structural basis of long-distance electron transfer and EPR spectroscopy

Structural determination of CntA revealed that the two functional domains in CntA (the Rieske domain and the catalytic mononuclear Fe domain) are located 44 Å apart in the same subunit. As such, electron transfer to the catalytic mononuclear Fe centre is likely to occur only at the interface of two adjacent CntA subunits (12.2 Å apart) and facilitated by the so-called bridging glutamate (E205, Figure 2A) (13). Electron transfer from NADH to the carnitine oxygenase CntA is mediate through an flavin mononucleotide (FMN)-containing reductase CntB, which was essential for the enzyme activity (13). To monitor electron transfer pathway (Figure 2B) from the reductant NADH via the flavin-containing reductase CntB to the catalytic domain in the oxygenase CntA, continuous wave (cw)-EPR was used.

Purified CntB is EPR-silent (Figure 2C**,** black trace); however, the reduced ferredoxin-centre in CntB is readily detectable once NADH is added (red trace). The EPR spectrum of reduced CntB has a characteristic reduced ferredoxin $[2Fe\text{-}2S]^{+1}$ signal [g tensor 2.031, 1.937, 1.899] and a radical signal resulted from flavin semiquinone g_{ave}=2.0015. Similar flavin semiquinone radicals have been observed previously in other Rieske oxygenase reductase as well as monoamine oxidase (35, 36). Reduced CntB spectrum was simulated by combination of two different S = ½ spin states (97 % for the reduced ferredoxin and 3 % for a flavin semiquinone radical) (Table 2), confirming electron transfer from the reductant NADH to the ferredoxin domain in CntB (steps 1-3 in Figure 2B). The purified CntA (blue trace) showed a very weak anisotropic EPR signal with $g_{ave} < 2.0$ [g tensor 2.011, 1.916, 1.757], indicating that the Rieske centre in CntA is predominantly in the oxidized, diferric $[2Fe\text{-}2S]^{2+}$ state (Table 2) (37-38). Addition of an oxidizing agent (H_2O_2) to CntA has minimal effect on the overall spectrum (*Figure S3A*), however, the Rieske centre in CntA can be readily reduced by dithionite (*Figure S3B*). CntA also appears capable of oxidising the

substrate (carnitine) using H_2O_2 in the absence of CntB/NADH (*Figure S3A*), consistent with the peroxide shunt-mechanism known in other Rieske oxygenases (39-40). In order to monitor electron flow from CntB to CntA, the spectrum of CntA +NADH+CntB was recorded (magenta trace). This complex spectrum can be simulated by the combination of three different S = ½ spin states (Table 2**,** *Figures S4*). Thus, the addition of CntB+NADH to CntA allowed reduction of the Rieske centre in CntA, confirming cross-subunit electron transfer from CntB to CntA (step 4 in Figure 2B).

We next sought to confirm the electron flow from the reduced Rieske cluster to the catalytic mononuclear Fe centre in CntA and investigate the critical role of the bridging E205 in electron transfer as suggested by the CntA structure (step 5 in Figure 2B). The E205 residue bridges the Rieske cluster on one subunit and the mononuclear Fe centre in the adjacent subunit (Figure 2A) (13, 41). None of the E205 mutants that we generated in this study were active (Figure 2D), with no major perturbations to the overall secondary structure as observed by circular dichroism (Figure 2E). As it is known that substrate-binding can be required for the activation of the catalytic mononuclear Fe centre to initiate catalysis (42-43), the substrate (carnitine) was added to the reaction and the EPR spectrum was monitored (Figure 2C, cyan trace). The spectrum shows no EPR signals at low magnetic fields, ruling out the presence of high-spin (S = 5/2 or 3/2) ferric species in the sample. However, strong isotropic (3350 G) and highly anisotropic EPR signals are observed between the magnetic fields of 3200-3900 G (Figure 2C). The observed g_{ave} < 2.0 (Table 2) strongly indicates that these EPR transitions likely arise predominantly from one-electron reduced $[2Fe\text{-}2S]^{+1}$ Rieske cluster in CntA and the isotropic signal at 3350 G is likely originated from a new organic radical species, which is formed during CntA catalysis in the presence of the substrate. The EPR simulation from these two S = ½ species (reduced Rieske cluster and a new organic radical species) reproduced the observed spectra (Table 2**,** *Figure S4*). The complete loss of reduced ferredoxin EPR signal from CntB, together with the formation of a novel organic radical species (isotropic signal seen at 3350 G) in CntA+CntB+NADH+carnitine suggests an efficient electron transfer to the catalytic mononuclear Fe in the wild-type CntA (step 5 in Figure 2B).

To further support this proposed electron transfer pathway, we compared EPR spectra of the E205A mutant with the wild-type CntA. Indeed, the EPR spectra are significantly different between E205A (Figure 2C, purple trace) and the wild-type CntA (cyan trace). The spectrum of the E205A mutant shows complex EPR signals with 4 different S = ½, EPR active species (Table 2). In the spectrum with the E205A mutant, a significant amount (60 %) of the EPR signal of the reduced $[2Fe\text{-}2S]^{1+}$ ferredoxin in CntB was observed while this was not found in the spectrum of the wild-type CntA, suggesting that electron flow is significantly impacted in this mutant. Together, the EPR observations provide strong evidence of each step involved in the electron flow as proposed in Figure 2B and confirm the role of the bridging glutamate (E205) in cross-subunit electron transfer as suggested by the CntA structure.

Structural basis of substrate binding and inhibition

CntA can catalyse the oxidation of carnitine and several substrate analogues (Figure 3A). The high resolution CntA structures co-crystalized with the ligands (carnitine, 2.0 Å; gBB, 1.6 Å) allowed us to define the

substrate binding pockets. The ligands were built into the clear density which was much better defined for the carnitine structure (Figure 3B). The substrate-binding site is formed by a series of β-sheets and two α-helices coordinating the substrate through hydrophobic/steric interactions involving residues Phe 258, Tyr 315, and Phe 319 and polar interactions with residues Tyr 225, Asn 270, and Tyr 295. (Figure 3C, *Figure S5*). The Phe 319 residue is positioned at the kink of an observed π-helix feature for residues 306 to 337 (44). Importantly, we also observe that Tyr 203 forms a π-cation interaction with the positively charged ammonium group in the substrates (Figure 3C). The importance of the binding site residues was then tested by mutating them to alanine. Indeed, all mutants decreased or abolished activity (Figure 3D). Interestingly, the Y203F mutant was active (Figure 3D), demonstrating a recovery of function and the pivotal role of the π-cation interaction with the ammonium group.

The presence of an aromatic residue in this position (Y203 or F203) appears to be restricted to CntA and several closely related enzymes. Indeed, a comprehensive phylogenetic analysis of Rieske oxygenases, including several other recently defined Rieske enzymes involved in the oxidation of quaternary ammonium substrates clearly defined a group which delineates quaternary ammonium Rieske oxygenases (group V) from the well-studied ring-hydroxylating Rieske oxygenases (Figure 4A) (27, 29). While group I-IV Rieske oxygenases primarily catalyse the dihydroxylation of aromatic and polyaromatic compounds that are important in bioremediation of environmental pollutants, group V Rieske oxygenases include enzymes that principally oxidise quaternary ammonium substrates (Figure 4B). Interestingly, based on the presence or absence of the signature aromatic residue at position 203 (Y203 or F203), group V Rieske oxygenases can be further separated into two clades Va and Vb where in clade Vb the Tyr (or Phe in OxyBAC) is replaced by an Asn (Figure 4C). Substrates for the former clade include carnitine (CntA, 13), choline (CmoA, CmoS, CmoB, 45-47) and benzalkonium (OxyBAC, 29) whereas the latter clade Vb enzymes undertake oxidative demethylation from the ammonium group for glycine betaine (GbcA, BmoA, 27) and proline betaine (stachydrine, Stc2, 28).

Comparing the ligand-bound structures of CntA (group Va) and Stc2 (group Vb) uncovers striking differences in the way quaternary amine substrates are oriented (28). In Stc2 the substrate analogue proline is ligated with the catalytic Fe through the carboxylate group (Figure 4D), whereas in CntA, although a carboxylate group is present, the substrates were oriented via a π-cation interaction with the trimethylammonium moiety and the carboxylate group is not ligated with the mononuclear Fe (Figure 3C).

In order to understand the substrate specificity for the enzyme, we investigated the structure activity relationship (SAR) of 22 substrate analogues with differences on the aliphatic chain, the carboxyl group or the amine terminal groups (Figure 5A, *Figure S6*). In addition to carnitine/γ-butyrobetaine (compound 1 and 2), CntA can also oxidise meldonium (compound 3) and 1-butyl-trimethylammonium (compound 4) albeit with a lower affinity (Figure 3A, Figure 5A). The lack of a carboxylic acid in compound 4 reduces the affinity for the substrate and substrates with longer alkyl chains or other functional groups showed no activity (compounds 5-9). A further series of compounds related to γ-butyrobetaine but

not quaternary ammonium salts (compounds 10- 12) did not serve as substrates for CntA. Other quaternary amine compounds tested were not accepted as substrates (*Figure S6*). Together, structural, mutagenesis and SAR data therefore suggest that the substrates for CntA are primarily co-ordinated through a π-cation interaction between Y203 and the trimethylammonium group, which positions the substrate in place above the mononuclear Fe site for oxidative cleavage to occur (Figure 5B). Although there is some tolerance for the lack of a carboxylic acid, increases in the length of the molecule and increased steric bulk are not favoured for enzyme activity as they likely disturb the polar interaction with Tyr 295.

A competitive inhibitor binds to the same substrate recognition pocket through π-π stacking interactions

Encouraged by previous success in the identification of substrate mimics as potent inhibitors for the choline-TMA lyase CutC (18-21), we also screened these carnitine analogues (Figure 5A, *Figure S6*) as potential inhibitors of CntA in competition assays. However, none of these substrate analogues inhibited CntA activity. We thus used a random approach by screening drug libraries and successfully obtained 3 inhibitor compounds MMV1, MMV3 and MMV12 (Figure 6A). Their inhibitory IC_{50} values are in the range of 1.1-5.8 µM (Figure 6B). From competition assay data (*Figure S7*) we were able to derive a K_i (1.09 µM) for MMV12 (ID, MMV020670), indicating that it is likely a competitive inhibitor.

We successfully solved the structure of MMV12 with CntA (PDB, 6ZGP) and indeed, the inhibitor occupied the substrate binding pocket (Figure 6D). Interestingly, Tyr 203 and Tyr 295, both of which are important for the coordination of carnitine in CntA (Figure 5B), also play a key role in binding to the inhibitor (*Figure S8)*. Tyr 203 form a π-π stacking interaction with the 1,6-naphthyridine core ring and Tyr 295 forms polar interaction with the oxygen on the methoxy group in the inhibitor. Interestingly, the inhibitor is also coordinated to the mononuclear Fe via a nitrogen on the 1,6-naphthyridine ring at distance of 2.65Å and to an oxygen of the carboxylic acid moiety of Asp 323 at 2.7Å (*Figure S8)*. Other π-π interactions are also observed between Phe 319 and the phenyl methoxy group and between Phe 258/ Phe 247 and the imidazole group. When the binding pockets of carnitine and MMV12 are compared (Figure 6E & F), Phe 258 moves to accommodate the imidazole group of the inhibitor whilst the loop containing Phe 216 is drawn in closer to the active site to form the π-π interaction with the inhibitor.

The two other inhibitors MMV1 and MMV3 share similar structural features to MMV12. MMV1 has a core bicyclic fused aromatic scaffold with two branching cyclic groups. MMV3 has an imidazole group with an aliphatic amine linker group. The remaining pair of inhibitors show more complex patterns of inhibition for CntA. Using the structure of CntA co-crystalized with MMV12, we applied *in silico* docking of MMV1 and MMV3 to observe if these molecules could adopt comparable poses (*Figure S9*). The results showed that both compounds show logical poses in the binding site with docking scores of -10.576 (kcal/mol) and -11.169 (kcal/mol), respectively. These are comparable to a score of -11.7 (kcal/mol) when MMV12 is docked into the empty pocket in CntA. Both docked compounds demonstrate likely coordination to the Fe centre via a nitrogen atom and similar π-π stacking interactions.

In order to assess the activity of these inhibitors, we monitored the impact

of these inhibitors on the production of TMA in *A. baumannii* cells pre-grown on carnitine. Indeed, we observed a decrease in TMA production in the presence of MMV3 and MMV12 (Figure 6C), whilst MMV1 did not inhibit TMA formation in the bacterial culture. MMV3 has almost completely inhibited TMA formation while MMV12 caused ~20% reduction in TMA production. It is worth mentioning that MMV3 was originally developed for treating tuberculosis and the differences in inhibitor activity towards *A. baumannii* cells may reflect their ability to penetrate bacterial cell membranes.

Discussion

A major breakthrough in gut microbiome research over the past decade is the realization that gut microbiota play an integral role in human health and diseases (48). This is exemplified in the study of TMA-formation from gut microbiota and its implication in the development of atherosclerosis and cardiovascular diseases (9-11). Recent progress using experimental animals and human clinical studies have shown that TMA precursors such as choline, carnitine and γ-butyrobetaine promote atherosclerosis via the TMAO pathway through the interplay between gut microbiota and host metabolism (49). The identification of the key microbial enzymes, including the choline-TMA lyase (12) and CntA (13) provides promising new drug targets for attenuating TMA release from gut microbial metabolism of TMA-precursors. Although much has been learnt from the structures of choline-TMA lyase and subsequent development of selective inhibitors for choline-to-TMA transformation (18-21), little progress has been made on CntA due to the lack of CntA structures. Here in this study, we provide the structural basis of substrate co-ordination and mode of inhibition by the newly discovered inhibitors. The structure and EPR analysis also allow us to better understand the structural basis of long-range electron transfer across the interface of CntA subunits.

Rieske oxygenases are challenging proteins to study and this was no different in the case of CntA. Different expression strategies or the choice of buffers and additives may have contributed to the apparent differences in enzyme activities among studies of CntA protein (13, 50). Due to sensitivity to oxygen, considerable effort was made in our work in order to obtain CntA crystals. It is worth noting that the presence of SCN in the crystallisation media was essential to obtain CntA crystals. Given that we observe the SCN coordinated to the Fe centre in CntA-carnitine and CntA-gBB complex, we investigated the effect of additional SCN on the activity of CntA. Indeed, SCN inhibited CntA activity with the half maximal inhibitory concentration (IC_{50}) of 35 mM (*Figure S10A*) and EPR analysis showed that the addition of SCN may have affected inter-/intra subunit electron transfer *(Figure S10B*). It is therefore likely that SCN affects CntA functionality by coordinating to the Fe centre and preventing oxygen binding, which in turn helps to stabilise the protein for crystallization.

Our study shows that CntA forms a head-to-tail homotrimer and the substrates appear to be poised in place next to the mononuclear Fe centre ready for cleavage. Despite both substrates (*i.e.* carnitine and γ-butyrobetaine) possessing carboxylate moieties, these are not coordinated to the mononuclear Fe centre as might be expected and that has been observed for group Vb Rieske oxygenase such as proline-bound stachydrine demethylase Stc2 (28). The Y203 residue is strictly conserved in all CntA sequences which is key for a π-cation interaction to coordinate the ammonium moiety of the

substrate and for a π-π stacking interaction to the inhibitor (Figure 6). This corresponding aromatic residue is also present in other group Va Rieske oxygenases, such as choline monooxygenase (tyrosine) and OxyBAC (phenylalanine) (Figure 4), suggesting that such a π-cation interaction is commonly used for orientating choline and benzalkonium during catalysis. Conversely, when compared to the stachydrine and glycine betaine degrading enzymes, Stc2 and BmoA/GbcA respectively, there is not an aromatic residue present in the same position. The structure for Stc2 showed that stachydrine coordinates to the mononuclear Fe through the carboxylate group and the suggested mechanism requires this binding mode in order to cleave the methyl substituent (28). This insight suggests a differentiation amongst the Group V members and thus a distinctive way to classify quaternary ammonium catalysis by such Rieske oxygenases.

Among the substrate analogues tested for CntA, activity was only seen in compounds containing a quaternary ammonium group, In agreement with the pivotal role of the π-cation interaction for substrate coordination. Given the link between TMA production and cardiovascular diseases, targeting CntA with small molecule inhibitors could have a therapeutic potential. Inhibitors for CntA may also be useful to treat individuals with a socially challenging condition trimethylaminuria (TMAU) or commonly referred to as the "fish odour syndrome" (51). An elegant example of such rational designed inhibitors starting from the endogenous substrate has been reported for the choline-TMA lyase, CutC with DMB (3,3-dimethyl-1-butanol), DMBA (3,3-dimethylbutyric aldehyde), FMC (N-(fluoromethyl)-2-hydroxy-N,N-dimethylethan-1-aminium) and (3S) - 1 - methyl - 3,6 - dihydro - 2H - pyridin - 3 - ol (18-21). FMC is reported as the most potent inhibitor with an EC_{50} of 56 nM by forming an irreversible covalent bond in the CutC catalytic site (20). Encouragingly and particularly relevant to CntA is the development of inhibitors based on the structure of γ-butyrobetaine against the carnitine-producing γ-butyrobetaine hydroxylase from human (52). The inhibitors were derivatives of the trimethylammonium, aliphatic chain and carboxylate region with some demonstrating a similar binding mode to the native substrate but with higher affinities. The structure of CntA, together with the information inferred from the substrate mimics and the competitive inhibitors that we reported here in this study, could be investigated in a rational drug design approach to formulate more potent CntA inhibitors for future exploitation. The data presented here suggest CntA substrate analogues are less likely to inhibit its activity and rational drug design should perhaps take advantage of the presence of several aromatic residues in the binding pocket to utilize a π-π stacking interaction as we have demonstrated in the inhibitor compound (Figure 6).

Taking advantage of the CntA structure we solved in this study, we employed EPR analysis to track the activation and progression of the electron transfer pathway involving the carnitine oxygenase complex. We propose that during catalysis, CntA and its associated reductase, CntB approach and electron transfer from the one-electron reduced ferredoxin $[2Fe\text{-}2S]^{+1}$ in CntB to the oxidized Rieske $[2Fe\text{-}2S]^{2+}$ effectively takes place. Efficient electron transfer from the reduced Rieske $[2Fe\text{-}2S]^{1+}$ centre to the catalytic mononuclear Fe centre in CntA requires both substrate, carnitine and the crucial bridging glutamate reside E205,

mutation of which significantly alters electron flow (Figure 2C), resulting in the loss of enzyme activity (Figure 2D). This was also independently validated by a recent study showing that both E205D and E205Q mutants lost enzyme activity and the ability for electron transfer to the active centre (13, 50). Binding of the substrate to the catalytic mononuclear Fe centre caused a shift in g_3 tensor from 3810 G to 3750 G (Figure 2C). This suggests that substrate entrance might influence the redox-potential of the mononuclear Fe centre in CntA, possibly influencing the electron transfer from the reduced Rieske centre to the mononuclear Fe centre in CntA although its impact on the one electron reduced Rieske centre cannot be completely ruled out. The terminal step of the electron transfer pathway is the formation of an organic radical species (Table 2) which is likely to be crucial for CntA catalysis. Its identity, however, has yet to be elucidated. Potential active intermediates in other well studied Rieske oxygenases include Fe(III)-(hydro)peroxy followed by a rearrangement leading to a high valent hydroxo-Fe(V)=O or Fe(IV)=O species (53-55). The active high valent catalytic Fe in CntA catalysis certainly warrants further investigations. However, the methodology established here may also facilitate the discovery of novel CntA inhibitors targeting the electron transfer pathway.

To sum up, this work provides the structural basis of carnitine degradation by CntA. Structural determination of CntA and spectroscopic characterisation using EPR provides structural and mechanistic insight into the role of bridging glutamate (E205) in inter-subunit electron transfer. Co-crystallisation of the substrates and the competitive inhibitor with CntA unveils the role of the π-π stacking interaction as the key mode of inhibition. The work presented here provides the structural basis to facilitate rational design and further optimization of specific inhibitors targeting carnitine-to-TMA transformation by gut microbiota.

Methods

Cloning of CntAB and site-directed mutagenesis of CntA. The plasmids for expressing CntA and CntB of *A. baumannii* were constructed previously (13). All *A. baumannii* CntA mutants were chemically synthesized by GenScript and cloned into the pET28a(+) expression vector using the NdeI and HindIII sites. All plasmids were transformed into BL21(DE3)pLysS cells for protein expression as described previously (13).

Protein expression and purification. For each respective protein, recombinant *E. coli* strains were streaked from glycerol stocks onto LB agar plates with kanamycin (50 µg/mL) and incubated overnight at 37°C. Recombinant protein expression was induced with 0.2 mM IPTG into liquid culture in LB medium. After 18 hours incubation the cells were collected by centrifugation at 6,000 rpm at 4°C for 10 minutes and the pellet was resuspended in 20mL PBS + 0.3M NaCl on ice, aliquoted and frozen at -80°C. For purification the standard buffer conditions were 20 mM Tris-HCl pH 7.6, 250 mM NaCl and 0.5 mM tris(2-carboxyethyl)-phosphine (TCEP). To purify CntA and CntB proteins, cells were broken by sonication in the standard buffer and the cell-free extract was loaded on a Roche Complete resin for affinity purification. The resin was then washed with standard buffer + 5 mM imidazole and the target protein was eluted with the standard buffer + 250 mM imidazole + 10% (v/v) glycerol. The elution was concentrated in a Vivaspin 20 10,000 kDa cut-off to 2.2 mL before loading onto a Superdex 200 16/600 column using an ÄKTA purifier and buffer exchanging into

10 mM HEPES, 250 mM NaCl, 0.5 mM TCEP and 10% glycerol (v/v) buffer for storage or 10 mM HEPES pH 7.6, 10 mM NaCl and 0.5 mM TCEP for crystal growth. For storage, the protein was concentrated to 2mg/mL in a Vivaspin 6 10,000 kDa and aliquots were kept frozen at -20°C, for crystallography the protein was concentrated to the desired amount (between 5 to 50 mg/mL) and used immediately in crystallisation setups. Purified CntB was estimated to have ~ 0.85 FMN per CntB using the method of Batie et al. (1987) by measuring absorbance at 462 nm against FMN standards ranging from 0.3 to 321.5 µM (35).

Protein crystallography. CntA crystals were seeded and obtained at 22°C using the hanging drop method. All drops contained 1µL of protein material and 1µL crystallisation condition. Initial crystallisation conditions were obtained from sparse matrix screening using JCSG-plus™ (Molecular Dimensions) and optimised using the Additive Screen (Hampton Research). Seeding material was generated with protein at 10-20 mg/mL in drops containing 100 mM HEPES, 0.2 M NaSCN, 20% (w/v) PEG 3350, 10 mM NaCl and 0.5 mM TCEP where large irregular crystals formed over 48 hours at 22°C. These crystals were scratched with acupuncture needles and then streaked through drops containing protein at 7.5 mg/mL 100 mM HEPES, 0.2 M NaSCN, 18% (w/v) PEG 3350, 10 mM NaCl and 0.5 mM TCEP with substrates (carnitine and γ-butyrobetaine) also present at a final concentration of 1 mM, the needle was run through 2 consecutive drops with a third drop on the cover slip as a control. Single red hexagonal crystals developed between 24 and 36 hours at 22°C and were collected immediately thereafter (prolonged incubation of the crystals was found to be detrimental to their crystal quality). Crystals were cryoprotected in an equivalent solution to the mother liquor supplemented with 5% glycerol and flash cooled in liquid nitrogen. For CntA+MMV020670, MMV020670 was added to a final concentration of 250 µM in the crystallisation condition buffer drops that were streaked and yielded the same red hexagonal crystals 36-48 hours after setting up. The crystals were collected and stored as mentioned above.

The crystals were mounted robotically on the i24 beamline (apo, carnitine and γ-butyrobetaine) and i04 beamline (CntA+MMV020670) at the Diamond Light Source (Harwell Science and Innovation Campus, Didcot, UK). In the apo and γ-butyrobetaine collections, we observed split spots and streaking of spots on some images. The apo, carnitine and MMV020670 data were auto-processed with Dials (56) using the Xia2 pipeline at Diamond Light Source followed by scaling with Aimless (57). For the γ-butyrobetaine dataset we processed the data using the Dials User Interface (DUI) followed by scaling with Aimless in the CCP4i2 suite of tools (58). An initial model was derived from PDB 3VCP. Molecular replacement was performed in PHASER. Autobuilding in phenix.autobuild was followed by iterative rounds of manual building in COOT (59) interspersed with refinement in PHENIX (60). Within Coot, monomers for L-carnitine (PDB code 152), γ-butyrobetaine (PDB code NM2), glycerol (GOL), thiocyanate (SCN) and HEPES (EPE) were added into clear density that was evident in both 2fo-fc and fo-fc maps consistent with the respective ligands. In order to assign the coordinates for MMV020670, Polder OMIT maps (61) were generated in PHENIX. Geometry restraint information as .cif file for MMV020670 was generated in eLBOW (62) within the PHENIX suite of programmes and the MMV020670

inhibitor was added into the model guided by Polder OMIT maps. The structure model coordinates can be accessed from the PDB repository with the following accession codes: CntA Apo (6Y8J), CntA + carnitine (6Y9D), CntA + gBB (6Y8S) and CntA+MMV020670 (6ZGP).

UV/VIS Enzyme assays. All activity assays were performed on a BMG FLOUstar Omega 96 well plate reader, set at wavelength 340 nm with a sample volume of 200 µL. The assay comprised of combining mixture A 60 µg CntA and 60 µg CntB with mixture B 0.25 mM L-carnitine and 0.25 mM NADH in a 10 mM HEPES buffer, pH 7.6 with 250 mM NaCl and 0.5 mM TCEP. The enzyme does not accept NADPH as the electron donor and the additional flavin (FAD or FMN) to the enzyme assay mixture had no major impact on enzyme activities (Figure S1). The reactions were measured for 5 minutes recording the linear decrease of signal at 340 nm for NADH oxidation. The slope of the line was measured between 60 and 120 seconds to yield the rate.

Michaelis–Menten kinetics. Michaelis–Menten kinetic parameters were derived using the UV/VIS Enzyme assays methodology above. Substrate concentrations were varied from a top concentration of 2 mM and decreasing in a 2-fold manner for 10 successive dilutions. Observed rates were obtained from 4 independent measurements and fitted to a nonlinear regression Michaelis-Menten model in Prism 8 for macOS v8.2.0.

Electron Paramagnetic Resonance (EPR) analysis. EPR measurements were carried out using a Bruker ELEXSYS-500/580 X-band EPR spectrometer operating in both continuous-wave (cw) and pulsed modes, equipped with an Oxford variable-temperature unit and ESR900 cryostat with Super High-Q resonator as reported previously (63-64). All EPR samples were prepared in the quartz capillary tubes (outer diameter; 4.0 mm, inner diameter 3.0 mm) and flash-frozen immediately and stored in liquid N_2 until analysis. The X-band EPR tubes were then transferred into the EPR probehead, which was pre-cooled to 20 K. The low-temperature EPR spectra were measured at 20 K as a frozen solution. A microwave power of 30 dB (0.2 mW) and modulation of 5 G appear to be optimal for recording the EPR spectrum of the CntA/CntB (oxygenase/reductase) domains prepared under various experimental conditions. The concentration of the CntA/CntB domains was 200 µM in all the samples. All experiments were carried out in 10 mM HEPES, pH 7.6, 250 mM NaCl, 10 % Glycerol and 0.5 mM TCEP, with additional NADH and or L-carnitine at a final concentration of 75 mM added accordingly. The analysis of the cw-EPR spectra and simulations were performed using EasySpin toolbox (5.2.18) for the Matlab program package (65).

Circular Dichroism. The proteins were buffer exchanged on a PD-10 column into a 0.2M sodium phosphate buffer with 0.01M NaCl at pH 7.0 and prepared at 0.1mg/mL final concentration. The samples were analysed on a JASCO J-1500 at 20°C using a 0.1mm path length quartz cuvette. Data was collected between 260 to 180 nm with 8 scans per sample collected.

Inhibitor screening assay. Compounds in the Pathogen Box (https://www.mmv.org/mmv-open/pathogen-box/about-pathogen-box) were received as 10 mM stocks dissolved in dimethylsulfoxide (DMSO). The compounds were added such that the final concentration was 50 µM in the 200 µL reaction. As per the "UV/VIS Enzyme

assays" methodology above, the protein in mixture A was incubated with inhibitor compounds for 20 minutes before commencing the assay. Compounds that demonstrated 25% or better inhibition relative to an untreated and equivalent DMSO control were further validated in two successive independent assays to confirm the inhibition activity to CntA.

Inhibitory IC_{50} determination. From a 25 mM stock solution of compound material dissolved in DMSO, a 3-fold, 10 step serial dilution was prepared and the final concentration of each compound ranges from 300 µM to 0.015 µM. The assay was carried out as per the "UV/VIS Enzyme assays" and "Inhibitor screening" methodology above and each compound was incubated with the protein material for 20 minutes prior to assaying. For each concentration, 4 replicates were carried out. IC_{50} values were determined using a built-in "Dose Response Inhibition" – [Inhibitor] vs. response model in Prism 8 for macOS v8.2.0.

Inhibitor Competition assays. As per the Michaelis Menton kinetics methodology above, we carried a series of 4 runs in the presence of (i) 0x (control), (ii)0.25x, (iii)1x and (iv)4x of the IC_{50} value for each inhibitor compound with 4 independent replicates for each run and fitted to a nonlinear regression Michaelis-Menten model in Prism 8 for macOS v8.2.0.

Evaluation of inhibitors in *A. baumannii* cell culture. *A. baumannii* cells were cultured overnight in the M9 minimal media at 37°C with 10 mM L-carnitine as the sole carbon source. The cells were then collected by centrifugation and washed twice in a buffer containing 10 mM HEPES, 1 mM NaCl (pH 7.6). After wash, the cells were resuspended in the same buffer to a density of OD_{600} of 0.4. The cells were aliquoted into 5mL per replicate and carnitine was added to a final concentration of 1 mM with/without the addition of the inhibitors (*i.e.* MMV1, MMV3 and MMV12) at a concentration of 200 µM. A corresponding DMSO only control was also included. These cells with appropriate treatments were incubated at 37°C for 1 hour. The supernatant was then obtained by filtering through a 0.2 µm filter and analysed by ion chromatography by quantifying TMA production and carnitine degradation as described previously (13).

Chemical structures and protein structure depictions. MarvinSketch was used for drawing, displaying and characterizing chemical structures (Marvin v19.10.0 for Mac, 2019, ChemAxon http://www.chemaxon.com). Reaction summaries were drawn in ChemDraw V17.0 for Mac. Molecular graphics and analyses were performed with UCSF Chimera (66), Chimera X (67) and Coot (59). Protein-ligand interaction maps were generated in Maestro (Academic) v11.9.010 Release 2019-1 – Schrodinger.

in silico docking. Structures were prepared in MarvinSketch, saved as .sdf files an imported in to Flare (Cresset) (v3.0). The CntA+MMV020670 pdb file was imported into Flare and minimised using the standard built-in protocols. The ligands were docked using the built-in docking engine using the MMV020670 ligand pose as a template.

Acknowledgements This work was supported by a Leverhulme trust research grant (RPG-2016-307). MS acknowledges The University of Manchester and MIB for financial supports. We acknowledge the generous support from the Malaria Medicines Venture for providing the Pathogen Box and follow up material for this work and Cerith Harries and Caroline

Stewart from the Media Preparation Service at the University of Warwick for help making various culture media and reagents.

Data availability: The structures of CntA and its ligand bound forms have been submitted to the PDB database (accession numbers 6Y8J, 6Y8S, 6Y9D and 6ZGP). All other data have been included in the manuscript.

Author contributions Y.C, A.C and T.D.H.B conceived the study. M.Q. performed protein expression, purification, X-ray crystallization, inhibitor design and testing. M.S. performed EPR measurements. E.D. and E. J. helped with inhibitor testing. M.Q. wrote the manuscript with significant input from all co-authors.

Conflict of interest: The authors declare no conflict of interest.

References

1. Koeth, R. A. *et al.* Intestinal microbiota metabolism of L-carnitine, a nutrient in red meat, promotes atherosclerosis. *Nature Medicine* **19**, 576-585, (2013).
2. Wang, Z. *et al.* Gut flora metabolism of phosphatidylcholine promotes cardiovascular disease. *Nature* **472**, 57-63, (2011).
3. Cani, P. D. Human gut microbiome: hopes, threats and promises. *Gut* **67**, 1716-1725, (2018).
4. Lynch, S. V. & Pedersen, O. The human intestinal microbiome in health and disease. *New England Journal of Medicine* **375**, 2369-2379, (2016).
5. Shreiner, A. B., Kao, J. Y. & Young, V. B. The gut microbiome in health and in disease. *Current opinion in gastroenterology* **31**, 69-75, (2015).
6. Zeisel, S. H. & Warrier, M. Trimethylamine N-oxide, the microbiome, and heart and kidney disease. *Annual Review of Nutrition* **37**, 157-181, (2017).
7. Tang, W. H. & Hazen, S. L. The gut microbiome and Its role in cardiovascular diseases. *Circulation* **135**, 1008-1010, (2017).
8. Jie, Z. *et al.* The gut microbiome in atherosclerotic cardiovascular disease. *Nature Communications* **8**, 845, (2017). https://doi.org/10.1038/s41467-017-00900-1
9. Brown, J. M. & Hazen, S. L. Microbial modulation of cardiovascular disease. *Nature Reviews Microbiology* **16**, 171-181, (2018).
10. Tang, W. H. W., Li, D. Y. & Hazen, S. L. Dietary metabolism, the gut microbiome, and heart failure. *Nature Reviews Cardiology* **16**, 137-154, (2019).
11. Schmidt, A. C. & Leroux, J.-C. Treatments of trimethylaminuria: where we are and where we might be heading. *Drug Discovery Today*, (2020).
12. Craciun, S. & Balskus, E. P. Microbial conversion of choline to trimethylamine requires a glycyl radical enzyme. *Proceedings of the National Academy of Sciences of the United States of America* **109**, 21307-21312, (2012).
13. Zhu, Y. *et al.* Carnitine metabolism to trimethylamine by an unusual Rieske-type oxygenase from human microbiota. *Proceedings of the National Academy of Sciences* **111**, 4268-4273, (2014).
14. Jameson, E. *et al.* Anaerobic choline metabolism in microcompartments promotes growth and swarming of *Proteus mirabilis*. *Environmental Microbiology* **18**, 2886-2898, (2016).
15. Jameson, E. *et al.* Metagenomic data-mining reveals contrasting microbial populations responsible for trimethylamine formation in human gut and marine ecosystems. *Microbial Genomics* **2**, e000080-e000080, (2016).
16. Bodea S, Funk MA, Balskus EP, Drennan CL. Molecular basis of C-N bond cleavage by the glycyl radical enzyme choline trimethylamine-lyase. *Cell Chem Biol.* 23:1206–1216 (2016).
17. Kalnins, G. *et al.* Structure and function of CutC choline lyase from human microbiota bacterium *Klebsiella pneumoniae*. *Journal of Biological Chemistry* **290**, 21732-21740, (2015).
18. Wang, Z. *et al.* Non-lethal inhibition of gut microbial trimethylamine production for the treatment of atherosclerosis. *Cell* **163**, 1585-1595, (2015).

19. Orman, M. *et al.* Structure-guided identification of a small molecule that inhibits anaerobic choline metabolism by human gut bacteria. *Journal of the American Chemical Society*, 141(1):33-37 (2018).
20. Roberts, A. B. *et al.* Development of a gut microbe-targeted nonlethal therapeutic to inhibit thrombosis potential. *Nature Medicine* **24**, 1407-1417, (2018).
21. Bollenbach, M., Ortega, M., Orman, M., Drennan, C. L. & Balskus, E. P. Discovery of a cyclic choline analog that inhibits anaerobic choline metabolism by human gut bacteria. *ACS Medicinal Chemistry Letters*, (2020). https://doi.org/10.1021/acsmedchemlett.0c00005
22. Wackett, L. P. Mechanism and applications of Rieske non-heme iron dioxygenases. *Enzyme and Microbial Technology* **31**, 577-587, (2002).
23. Barry, S. M. & Challis, G. L. Mechanism and catalytic diversity of rieske non-heme iron-dependent oxygenases. *ACS Catalysis* 3(10):2362–2370 (2013).
24. Bugg, T. D. & Ramaswamy, S. Non-heme iron-dependent dioxygenases: unravelling catalytic mechanisms for complex enzymatic oxidations. *Current Opinion in Chemical Biology* **12**, 134-140, (2008).
25. Perry, C., de Los Santos, E. L. C., Alkhalaf, L. M. & Challis, G. L. Rieske non-heme iron-dependent oxygenases catalyse diverse reactions in natural product biosynthesis. *Natural Product Reports* **35**, 622-632, (2018).
26. Karlsson, A. *et al.* Crystal structure of naphthalene dioxygenase: side-on binding of dioxygen to Iron. *Science* **299**, 1039, (2003).
27. Shao, Y. H. *et al.* Glycine betaine monooxygenase, an unusual Rieske-type oxygenase system, catalyzes the oxidative N-demethylation of glycine betaine in *Chromohalobacter salexigens* DSM 3043. *Applied and Environmental Microbiology* **84**, (2018). DOI: 10.1128/AEM.00377-18
28. Daughtry, K. D. *et al.* Quaternary ammonium oxidative demethylation: X-ray crystallographic, resonance Raman, and UV-visible spectroscopic analysis of a Rieske-type demethylase. *Journal of the American Chemical Society* **134**, 2823-2834, (2012).
29. Ertekin, E., Konstantinidis, K. T. & Tezel, U. A Rieske-type oxygenase of *Pseudomonas* sp. BIOMIG1 converts benzalkonium chlorides to benzyldimethyl amine. *Environmental Science & Technology* **51**, 175-181, (2017).
30. D'Ordine, R. L. *et al.* Dicamba monooxygenase: structural insights into a dynamic Rieske oxygenase that catalyzes an exocyclic monooxygenation. *Journal of Molecular Biology* **392**, 481-497, (2009).
31. Hegg, E. L. & Jr, L. Q. The 2-His-1-carboxylate facial triad — An emerging structural motif in mononuclear non-heme iron(II) enzymes. *European Journal of Biochemistry* **250**, 625-629, (1997).
32. Wolfe, M. D., Parales, J. V., Gibson, D. T. & Lipscomb, J. D. Single turnover chemistry and regulation of O_2 activation by the oxygenase component of naphthalene 1,2-dioxygenase. *Journal of Biological Chemistry* **276**, 1945-1953, (2001).
33. Quaroni, L. G. *et al.* Interaction of nitric oxide with cytochrome P450 BM3. *Biochemistry* **43**, 16416-16431, (2004).
34. Cooper, C. E. Nitric oxide and iron proteins. *Biochimica et Biophysica Acta (BBA) - Bioenergetics* **1411**, 290-309, (1999).

35. Batie C.J., LaHaie E., Ballou D.P. Purification and characterization of phthalate oxygenase and phthalate oxygenase reductase from *Pseudomonas cepacia. J Biol Chem*. 262, 1510-1518, (1987).
36. DeRose V.J., Woo J. C. G., Hawe W. P., Hoffman B.M., Silverman R.B., Yelekci K. Observation of a flavin semiquinon in the resting state of monoamine oxidase B by electron paramagnetic resonance and electron nuclear double resonance spectroscopy. *Biochem*. 35, 11085-11091. (1996).
37. Lee, J., Simurdiak, M. & Zhao, H. Reconstitution and characterization of aminopyrrolnitrin oxygenase, a Rieske N-oxygenase that catalyzes unusual arylamine oxidation. *Journal of Biological Chemistry* **280**, 36719-36727, (2005).
38. Rosche, B., Fetzner, S., Lingens, F., Nitschke, W. & Riedel, A. The 2Fe2S centres of the 2-oxo-1,2-dihydroquinoline 8-monooxygenase from Pseudomonas putida 86 studied by EPR spectroscopy. *Biochimica et Biophysica Acta (BBA) - Protein Structure and Molecular Enzymology* **1252**, 177-179, (1995).
39. Wolfe, M. D. & Lipscomb, J. D. Hydrogen peroxide-coupled cis-diol formation catalyzed by naphthalene 1,2-dioxygenase. *Journal of Biological Chemistry* **278**, 829-835, (2003).
40. Neibergall, M. B., Stubna, A., Mekmouche, Y., Münck, E. & Lipscomb, J. D. Hydrogen peroxide dependent cis-dihydroxylation of benzoate by fully oxidized benzoate 1,2-dioxygenase. *Biochemistry* **46**, 8004-8016, (2007).
41. Pinto, A., Tarasev, M. & Ballou, D. P. Substitutions of the “bridging” aspartate 178 result in profound changes in the reactivity of the rieske center of phthalate dioxygenase. *Biochemistry* **45**, 9032-9041, (2006).
42. Pavel, E. G., Martins, L. J., Ellis, W. R. & Solomon, E. I. Magnetic circular dichroism studies of exogenous ligand and substrate binding to the non-heme ferrous active site in phthalate dioxygenase. *Chemistry & Biology* **1**, 173-183, (1994).
43. Rogers, M. S. & Lipscomb, J. D. Salicylate 5-hydroxylase: intermediates in aromatic hydroxylation by a Rieske monooxygenase. *Biochemistry* **58**, 5305-5319, (2019).
44. Fodje, M. N. & Al-Karadaghi, S. Occurrence, conformational features and amino acid propensities for the π-helix. *Protein Engineering, Design and Selection* **15**, 353-358, (2002).
45. Rathinasabapathi, B. *et al.* Choline monooxygenase, an unusual iron-sulfur enzyme catalyzing the first step of glycine betaine synthesis in plants: Prosthetic group characterization and cDNA cloning. *Proceedings of the National Academy of Sciences* **94**, 3454, (1997).
46. Burnet, M. & Hanson, A. D. Evidence that spinach choline monooxygenase is an iron-sulfur protein. *Plant Physiology* **108**, 42-42, (1995).
47. Burnet, M., Lafontaine, P. J. & Hanson, A. D. Assay, purification, and partial characterization of choline monooxygenase from spinach. *Plant Physiology* **108**, 581-588, (1995).
48. Berg, G. *et al.* Microbiome definition re-visited: old concepts and new challenges. *Microbiome* **8**, 103, (2020).
49. Zhu, W. *et al.* Flavin monooxygenase 3, the host hepatic enzyme in the metaorganismal trimethylamine N-oxide-generating pathway, modulates platelet

responsiveness and thrombosis risk. *Journal of Thrombosis and Haemostasis* **16**, 1857-1872, (2018).

50. Massmig M, et al. Carnitine metabolism in the human gut: characterization of the two-component carnitine monooxygenase CntAB from *Acinetobacter baumannii. J Biol Chem* 37:13065-13078.
51. Fennema, D., Phillips, I. R. & Shephard, E. A. Trimethylamine and trimethylamine N-Oxide, a flavin-containing monooxygenase 3 (FMO3)-mediated host-microbiome metabolic axis implicated in health and disease. *Drug Metabolism and Disposition* **44**, 1839, (2016).
52. Tars, K. *et al.* Targeting carnitine biosynthesis: discovery of new inhibitors against γ-butyrobetaine hydroxylase. *Journal of Medicinal Chemistry* **57**, 2213-2236, (2014).
53. Kovaleva, E. G., Neibergall, M. B., Chakrabarty, S. & Lipscomb, J. D. Finding intermediates in the O_2 activation pathways of non-heme iron oxygenases. *Accounts of Chemical Research* **40**, 475-483, (2007).
54. Kovaleva, E. G. & Lipscomb, J. D. Versatility of biological non-heme Fe(II) centers in oxygen activation reactions. *Nature Chemical Biology* **4**, 186-193, (2008).
55. Groves, J. T. High-valent iron in chemical and biological oxidations. *Journal of Inorganic Biochemistry* **100**, 434-447, (2006).
56. Winter, G. *et al.* DIALS: implementation and evaluation of a new integration package. *Acta Crystallographica Section D* **74**, 85-97, (2018).
57. Evans, P. R. & Murshudov, G. N. How good are my data and what is the resolution? *Acta Crystallographica Section D* **69**, 1204-1214, (2013).
58. Winn, M. D. *et al.* Overview of the CCP4 suite and current developments. *Acta Crystallographica Section D* **67**, 235-242, (2011).
59. Emsley, P., Lohkamp, B., Scott, W. G. & Cowtan, K. Features and development of Coot. *Acta Crystallographica Section D* **66**, 486-501, (2010).
60. Liebschner, D. *et al.* Macromolecular structure determination using X-rays, neutrons and electrons: recent developments in Phenix. *Acta Crystallographica Section D* **75**, 861-877, (2019).
61. Liebschner, D. *et al.* Polder maps: improving OMIT maps by excluding bulk solvent. *Acta Crystallographica Section D* **73**, 148-157, (2017).
62. Moriarty, N. W., Grosse-Kunstleve, R. W. & Adams, P. D. electronic Ligand Builder and Optimization Workbench (eLBOW): a tool for ligand coordinate and restraint generation. *Acta Crystallographica Section D* **65**, 1074-1080, (2009).
63. Karuppiah, V. *et al.* Structural basis of catalysis in the bacterial monoterpene synthases linalool synthase and 1,8-cineole synthase. *ACS Catalysis* **7**, 6268-6282, (2017).
64. Hedison, T. M., Heyes, D. J., Shanmugam, M., Iorgu, A. I. & Scrutton, N. S. Solvent-slaved protein motions accompany proton coupled electron transfer reactions catalysed by copper nitrite reductase. *Chemical Communications* **55**, 5863-5866, (2019).
65. Hemminga, M. A. & Berliner, L. *ESR Spectroscopy in membrane biophysics*. (Springer US, 2007).

66. Pettersen, E. F. *et al.* UCSF chimera - A visualization system for exploratory research and analysis. *Journal of Computational Chemistry* **25**, 1605-1612, (2004).
67. Goddard, T. D. *et al.* UCSF ChimeraX: meeting modern challenges in visualization and analysis. *Protein Science* **27**, 14-25, (2018).
68. Kumar, S., Stecher, G. & Tamura, K. MEGA7: Molecular evolutionary genetics analysis version 7.0 for bigger datasets. *Molecular Biology and Evolution* **33**, 1870-1874, (2016).

Table 1 X-ray data collection and refinement statistics.

Name	CntA Apo	CntA + Carnitine	CntA + gBB	CntA+MMV12
PDB code	**6Y8J**	**6Y8S**	**6Y9D**	**6ZGP**
Wavelength (Å)	1.7	1.3	1.3	0.9
Resolution range (Å)	40.1 - 2.05 (2.12 - 2.05)	81.42 - 1.97 (2.04 - 1.97)	39.78 - 1.63 (1.69 - 1.63)	78.64 - 2.01 (2.08 - 2.01)
Space group	P 63	P 1 21 1	P 63	P 1 21 1
Unit cell	91.6 91.6 82.96 90 90 120	91.59 177.77 158.8 90 90.17 90	91.16 91.16 81.47 90 90 120	91.07 173.77 157.29 90 90.15 90
Total reflections	224999 (13603)	1180725 (105398)	203443 (9804)	2229436 (218489)
Unique reflections	24714 (2443)	353116 (35196)	47465 (4434)	322879 (32095)
Multiplicity	9.1 (5.6)	3.3 (3.0)	4.3 (2.2)	6.9 (6.8)
Completeness (%)	99.3 (99.2)	98.8 (98.4)	98.8 (93.4)	99.4 (99.1)
Mean I/sigma(I)	7.41 (1.14)	5.2 (1.21)	6.8 (1.13)	6.9 (1.13)
Wilson B-factor (Å^2)	38	31	24	33
R-merge	0.189 (1.429)	0.149 (0.958)	0.134 (0.755)	0.165 (1.783)
R-meas	0.200 (1.575)	0.178 (1.168)	0.152 (0.967)	0.179 (1.929)
R-pim	0.064 (0.651)	0.096 (0.660)	0.070 (0.595)	0.068 (0.733)
$CC_{1/2}$	0.994 (0.438)	0.984 (0.638)	0.982 (0.517)	0.996 (0.698)
CC*	0.999 (0.781)	0.996 (0.883)	0.996 (0.825)	0.999 (0.907)
Reflections used in refinement	24704 (2441)	352719 (35160)	47464 (4434)	321994 (31973)
Reflections used for R-free	1223 (101)	17582 (1828)	2374 (221)	16243 (1504)
R-work	0.201 (0.429)	0.207 (0.338)	0.1704 (0.323)	0.216 (0.386)
R-free	0.248 (0.530)	0.243 (0.371)	0.193 (0.339)	0.254 (0.421)
CC(work)	0.958 (0.737)	0.961 (0.805)	0.963 (0.726)	0.961 (0.799)
CC(free)	0.942 (0.821)	0.953 (0.760)	0.911 (0.768)	0.948 (0.736)
Number of non-hydrogen atoms	2874	35752	3117	36701
macromolecules	2803	34344	2832	34901

ligands	4	408	31	588
solvent	67	1000	254	1212
Protein residues	345	4224	350	4328
RMS(bonds) (Å)	0.008	0.009	0.007	0.009
RMS(angles) (°)	1.18	1.10	1.05	1.32
Ramachandran favored (%)	94.67	95.35	95.91	94.76
Ramachandran allowed (%)	5.33	4.50	3.80	4.98
Ramachandran outliers (%)	0.00	0.14	0.29	0.26
Rotamer outliers (%)	0.00	0.87	0.00	0.85
Clashscore	5.86	9.36	3.41	13.20
Average B-factor (Å^2)	55.95	45.44	35.71	51.59
Macromolecules (Å^2)	56.24	45.40	34.94	51.60
[2Fe-2S] Rieske Centre	44.74	41.35	25.56	48.08
Fe	N/A	45.15	176.41	56.77
Substrate	N/A	47.02	57.75	N/A
Inhibitor	N/A	N/A	N/A	69.75
Solvent (Å^2)	44.69	39.21	42.61	44.22
Number of TLS groups	9	48	10	44

Table 2 Spin-Hamiltonian parameters used to model the EPR spectra.

Samples	EPR active signal	species	%	g_1	g_2	g_3	g_{ave}
As-isolated CntA				2.0105	1.9157	1.7574	1.8945
As-isolated CntB	No EPR active signal detected						
CntB+NADH	$[2Fe\text{-}2S]^{+1}$	specA (reduced ferredoxin domain)	93	2.0312	1.9372	1.8988	1.9558
	Flavin radical	specB (Flavin radical)	7	2.0015	2.0015	2.0015	2.0015
CntA+CntB+NADH	$[2Fe\text{-}2S]^{+1}$ in CntB	specA (reduced ferredoxin domain)	61	2.0313	1.9376	1.8979	1.9556
	Flavin radical	specB	2	2.0010	2.0034	2.0039	2.0028
	$[2Fe\text{-}2S]^{+1}$ in CntA	specC (reduced Rieske centre)	37	2.0079	1.9153	1.7542	1.8924
CntA+CntB+NADH+Carnitine	an organic radical	specB	34	2.0000	2.0035	2.0037	2.0024
	$[2Fe\text{-}2S]^{+1}$ in CntA [A]	specC	66	2.0072	1.9077	1.7986	1.9045
E205A+CntB+NADH+Carnitine	$[2Fe\text{-}2S]^{+1}$ in CntB	specA1	40	2.0338	1.9397	1.8868	1.9534
	$[2Fe\text{-}2S]^{+1}$ in CntB	specA2	20	2.0449	1.9493	1.9037	1.9660
	Flavin radical [B]	specB	8	2.0012	2.0040	2.0040	2.0031
	$[2Fe\text{-}2S]^{+1}$ in CntA [A]	specC	32	2.0070	1.9077	1.7896	1.9014

[A] This EPR active signal may also contain an overlapping EPR-signals derived from the catalytic mononuclear iron centre; plausible EPR active intermediates are ferric-(hydro)peroxy or a high-valent iron(V)-oxo species.

[B] This may represent an overlay of both a flavin and an unidentified organic radical.

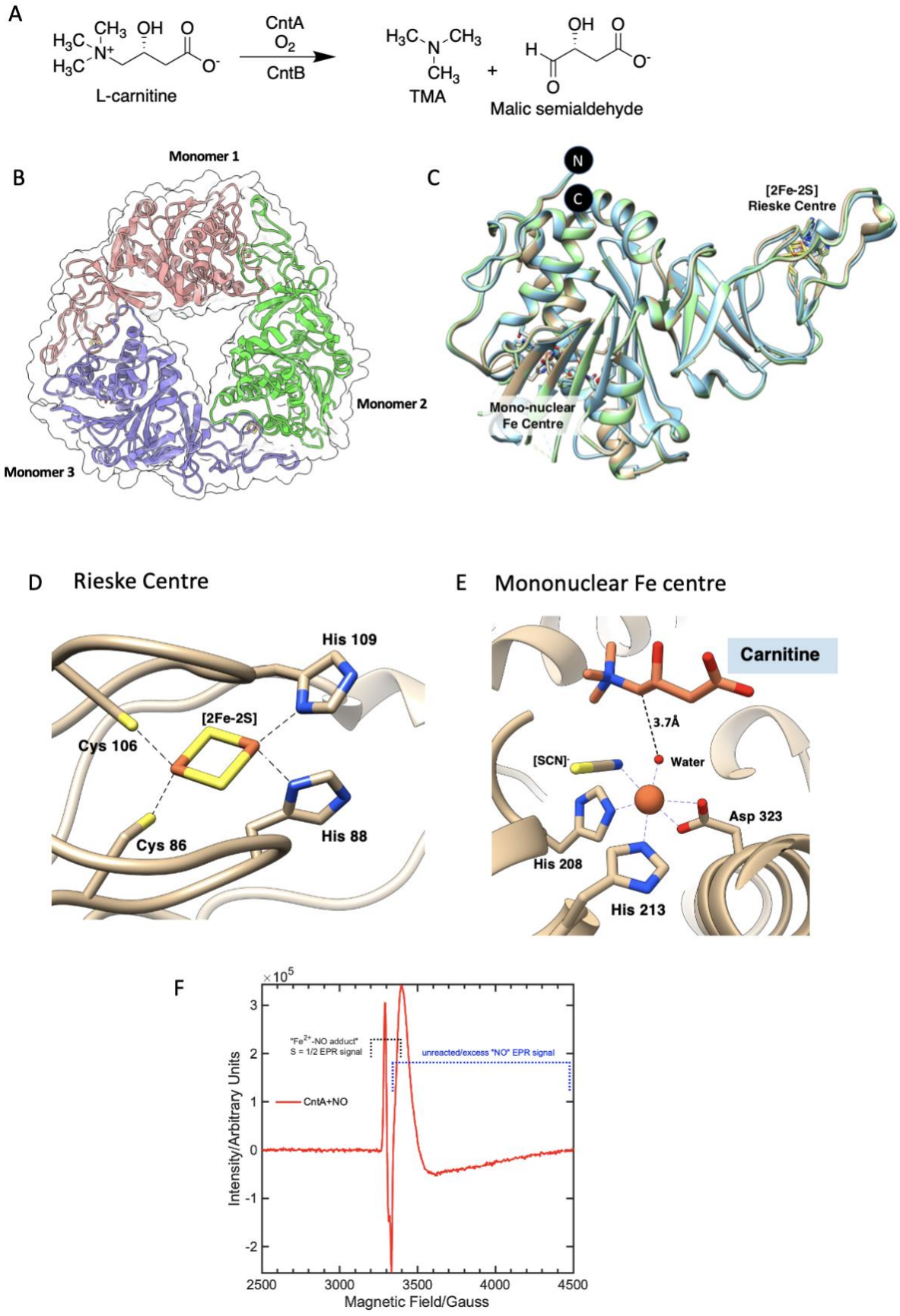

Figure 1 The overall structure of CntA and its catalytic centre.

A, The reaction of carnitine oxidation by CntAB to trimethylamine (TMA) and malic semialdehyde.

B, CntA depicted as a homotrimer with the secondary structure represented in a ribbon depiction in a translucent overall surface representation with each monomer in blue, red and green, respectively.

C, An overlap of three monomer structure units (apo, carnitine-bound, gBB-bound), showing no major changes to the tertiary structure of CntA with and without ligands bound. The C and N labels refer to the sequence termini. The Rieske centre and the mononuclear Fe centre are 44 Å apart in the same subunit.

D, The Rieske centre in CntA is coordinated by Cys86, Cys106, His88 and His109.

E, The catalytic mononuclear Fe centre in CntA is coordinated by a His-His-Asp catalytic triad (His208, His213, Asp323), a water and thiocyanate ion. Carnitine is shown above the mononuclear Fe centre with a distance from the water molecule to the site of substrate cleavage.

F, Electron paramagnetic resonance (EPR) spectra of as isolated CntA in the presence of nitric oxide (NO), showing the EPR-active, $S = ½$ species due to the formation of Fe^{2+}-NO adduct**.**; EPR conditions; microwave power 30 dB, modulation amplitude 5 G, time constant 81 ms, conversion time 41 ms, sweep time 84 s, receiver gain 60 dB, average microwave frequency 9.384 GHz, temperature 20 K.

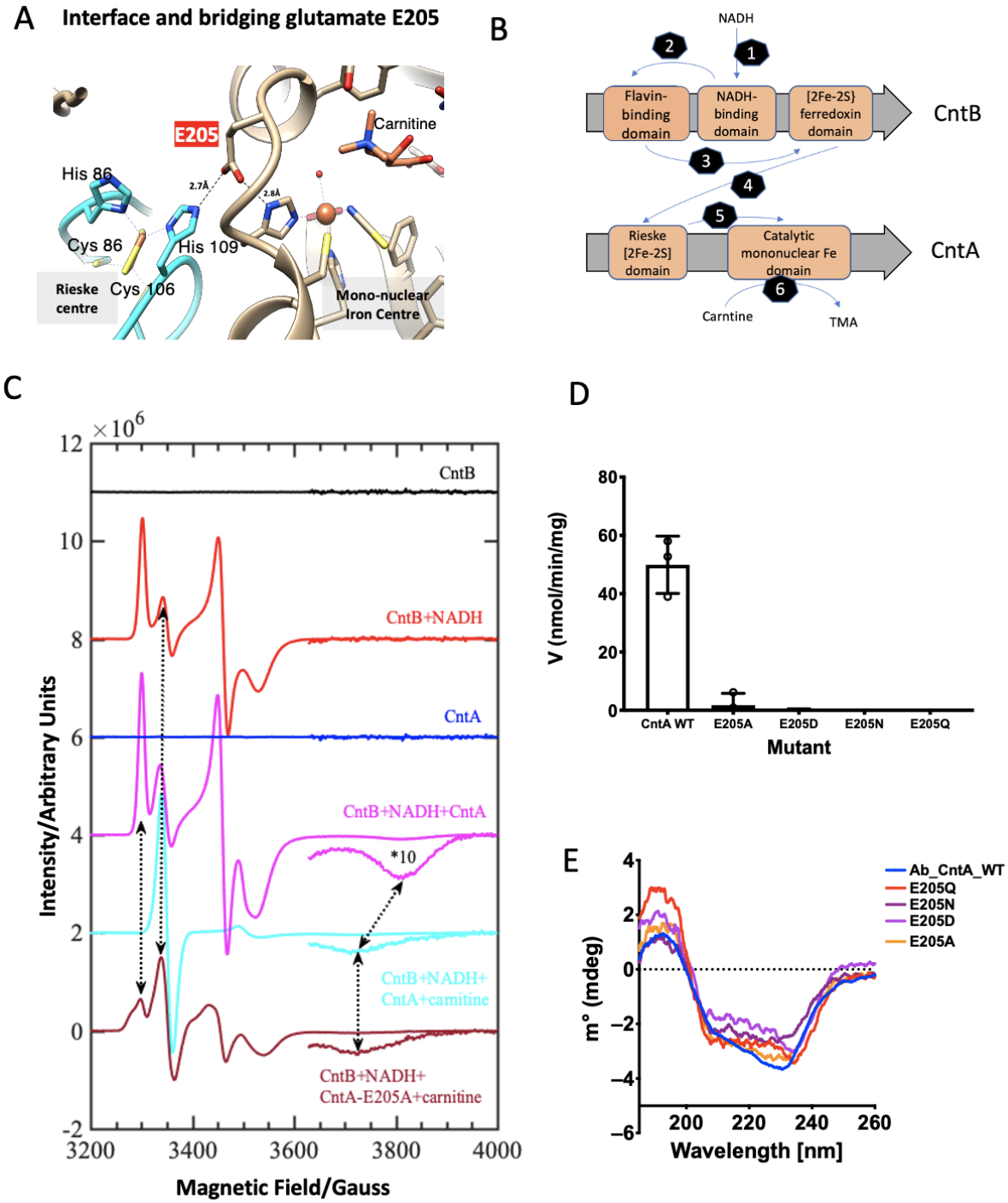

Figure 2 Structural basis of inter-subunit electron transfer and investigations by EPR.

A, Electron transfer in CntA between the Rieske centre and the mononuclear Fe centre across the interface of two neighbouring CntA subunits (coloured in cyan and brown, respectively) involved a key bridging glutamate reside (E205). Distances shown in Å.

B, Proposed electron transfer pathways from the reductant NADH to the catalytic mononuclear Fe centre in CntA via the reductase CntB.

C, EPR spectra of a series of combinations of WT CntAB proteins, E205A mutant, NADH and L-carnitine to track the propagation of EPR signal and thus the inter/intra subunit electron transfer. NADH reduction in CntB (black trace to red trace; steps 2 and 3 in Fig. 2B); the EPR active $[2Fe\text{-}2S]^{+1}$ species in the CntA Rieske centre with and without carnitine present

(red trace to magenta trace and cyan trace; steps 4-6 in Fig. 2B). The E205A mutant (wine red trace) demonstrates an EPR signal different to that of the wild-type CntA (cyan trace), indicating a disruption to the electron transfer pathway; EPR conditions; as in Fig 1E.

D, Activity assays of CntA E205 mutants.

E, Circular dichroism measurement comparisons between CntA wild type and E205 mutant enzymes showing no difference in secondary structure.

A

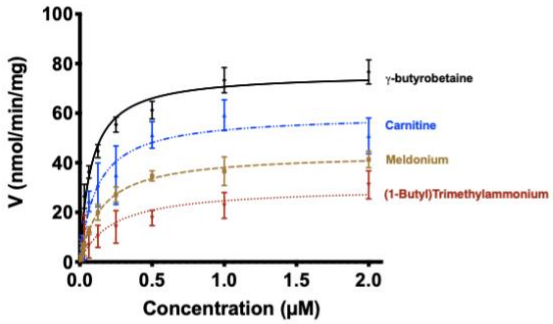

Substrate	Vmax (nmol/min/mg)	Km (nM)
Carnitine	59.0 (± 3.1)	117 (± 2.2)
γ-butyrobetaine	76.06 (± 1.6)	77 (± 1.0)
Meldonium	43.8 (± 1.4)	152.0 (± 1.7)
(1-Butyl) Trimethylammonium	30.1 (± 3.4)	222.0 (± 8.1)

B

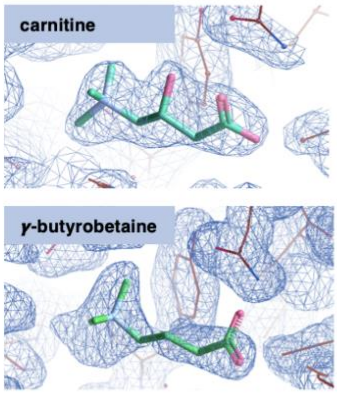

C

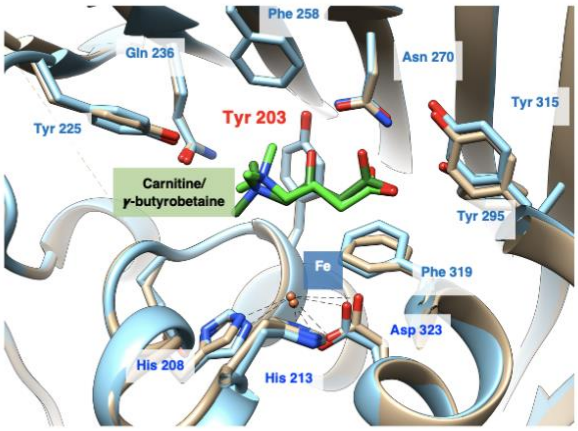

D

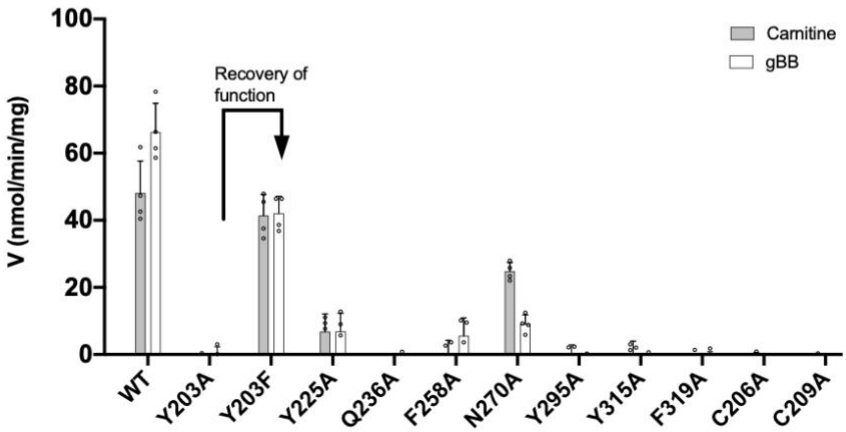

Figure 3 CntA substrate binding pocket.

A, Michaelis-Menten kinetics of CntA (n=4).

B, $2mF_o - DF_c$ map at 1.5σ maps (Blue) of carnitine displayed at 3.0σ and γ-butyrobetaine (gBB) displayed at 2.5σ.

C, Carnitine and γ-butyrobetaine interacting residues in the active site amongst which Y203 interacts with the substrate of CntA through the π-cation interaction.

D, Enzyme activity of site-directed mutants of key residues involved in substrate coordination in CntA from N=3 independent replicates. The Y203F mutant in CntA regains activity alluding to the crucial role of the aromatic system for a π-cation interaction.

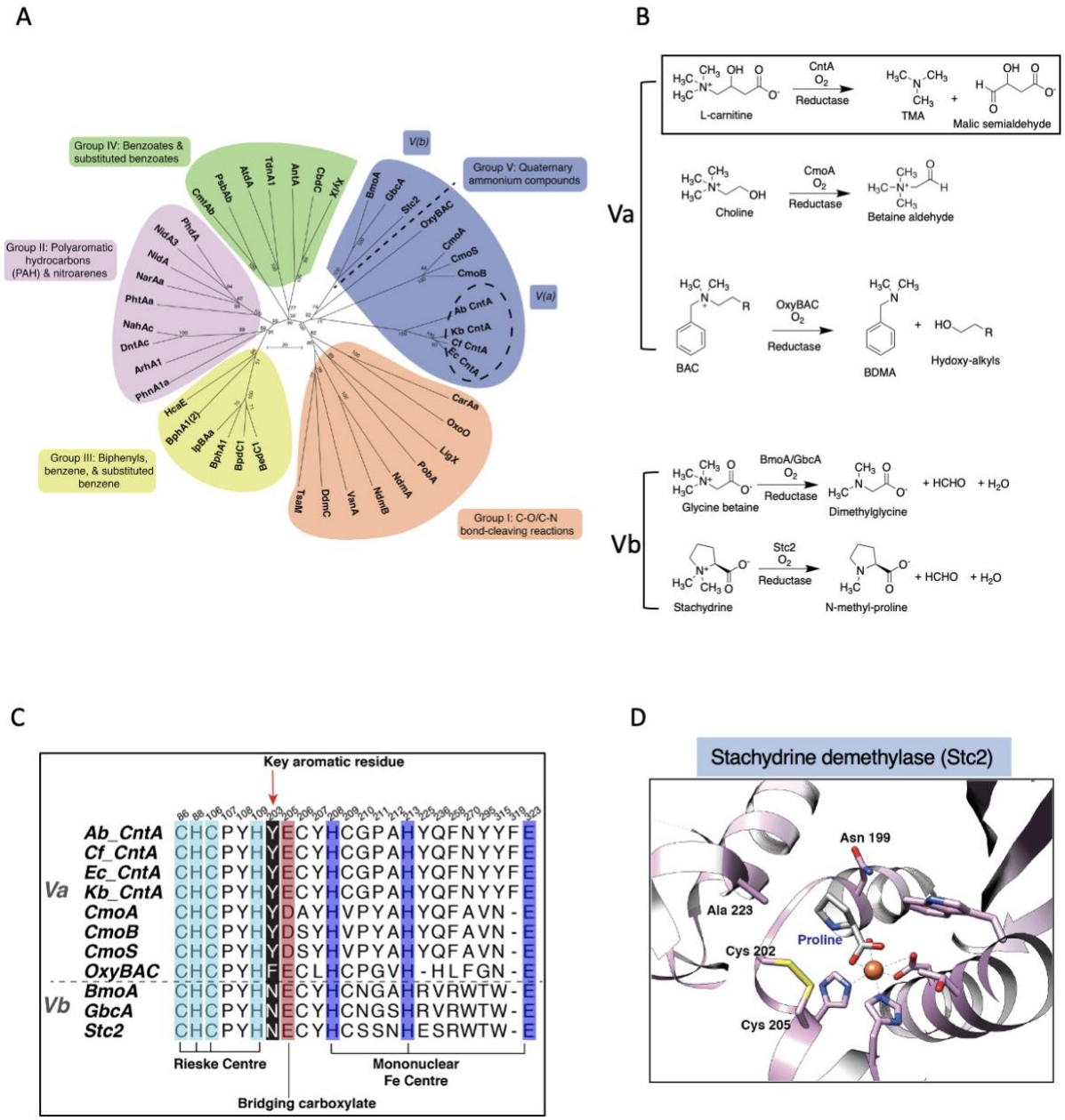

Figure 4 CntA represents a novel group of Rieske oxygenases using quaternary amine substrates (group V).

A, Phylogeny of Rieske oxygenases showing the five distinct groups. The evolutionary history of Rieske oxygenases was inferred using the Neighbour-Joining method in MEGA7 (68). The dashed circle grouping shows the clustering of CntA including *Acinetobacter baumannii* (Ab), *Escherichia coli* SE11 (Ec), *Klebsiella pneumonia* (Kb) and *Citrobacter freundii* (Cf) (See supplementary information, Appendix 1 for a list of gene accession ID's). Group V Rieske oxygenases oxidise quaternary amine substrates, including carnitine (CntA), choline (CmoA/B/C), benzalkonium (OxyBAC), glycine betaine (BmoA, GbcA) and stachydrine (Stc2).

B, Chemical reactions catalysed by Rieske enzymes from the Group V Rieske oxygenases involved in quaternary amine oxidations. Group Va includes carnitine oxygenase (CntA) choline monooxygenase (CmoA, CmoS and CmoB) and benzalkonium oxygenase (OxyBAC). Group Vb carries out oxidative demethylation reactions.

C, Sequence alignment of the substrate binding pocket residues of group V Rieske oxygenase involved in quaternary amine oxidation. The aromatic residues for substrate coordination through a π-cation in group Va and the corresponding position in group Vb are highlighted by a red arrow. The Rieske centre is coded in blue, the catalytic triad of the mononuclear Fe centre is shown in purple and the bridging carboxylate is highlighted in pink.

D, The substrate binding site of the group Vb quaternary amine degrading enzyme Stc2. The substrate mimic proline in Stc2 coordinates with the catalytic mononuclear Fe centre via a carboxylic acid group.

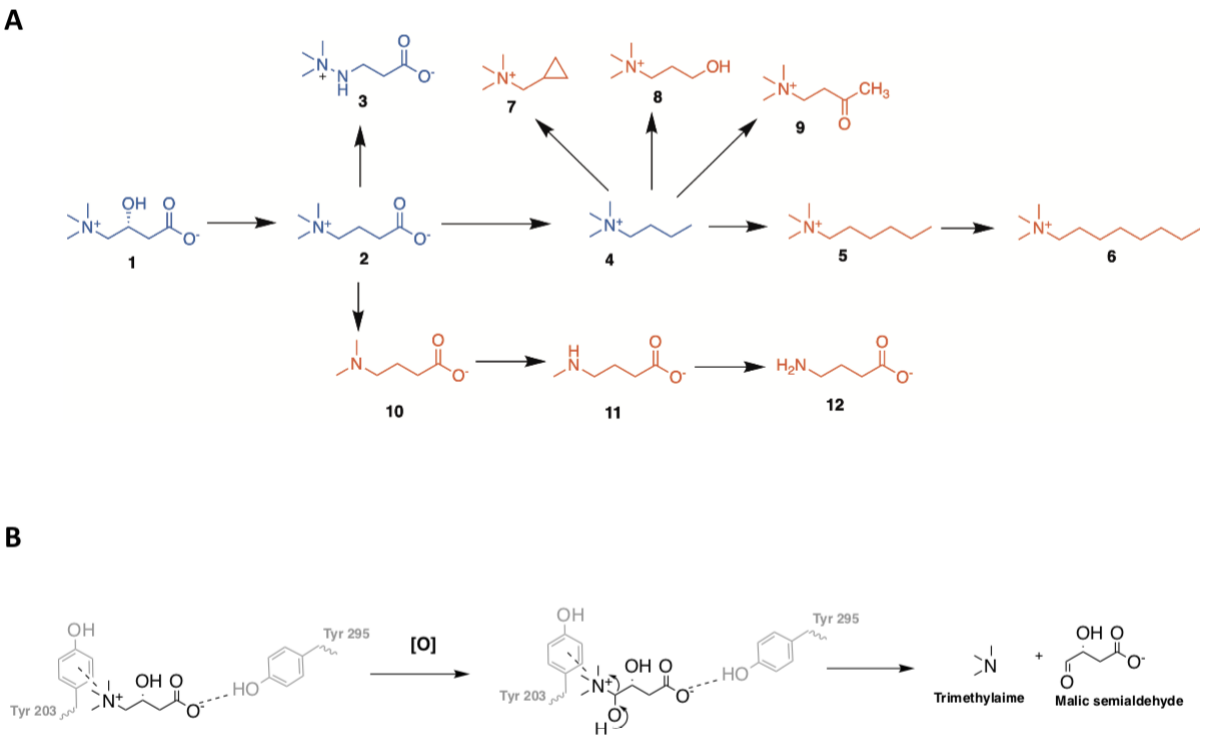

Figure 5 Structure activity relationship of CntA substrate profiling and coordination during catalysis.

A: A structure activity relationship scaffold hopping map of substrate analogues tested with a single change between structures and the progression shown with arrows. Structures in blue represent active substrates, whilst those in red are inactive. (**1**) Carnitine, (**2**) g-BB, (**3**) Meldonium, (**4**) (1-Butyl)Trimethylammonium, (**5**) (1-Hexyl)Trimethylammonium, (**6**) (1-Octyl)Trimethylammonium, (**7**) (Cyclopropylmethyl)-Trimethylammonium, (**8**) (3-Hydroxypropyl)Trimethylammonium, (**9**) (3-Oxobutyl)Trimethylammonium, (**10**) 4-(Dimethylamino)butyric acid, (**11**) 4-(Methylamino)butyric acid and (**12**) gamma-Aminobutyric acid.

B, The coordination of quaternary amine substrates in the CntA binding site during catalysis showing the role played by Tyr 203 and Tyr 295 in coordinating the substrates.

A

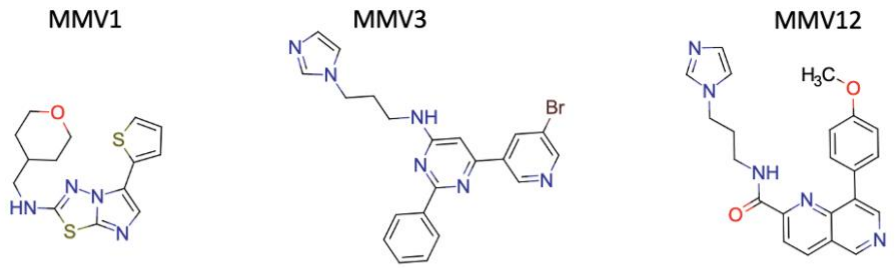

B

Inhibitor	MMV ID	Inhibitory IC_{50} (µM)	K_i (µM)	Original target
MMV1	MMV010764	5.8 (±1.1)	N/A	Malaria
MMV3	MMV661713	1.1 (±0.1)	N/A	Tuberculosis
MMV12	MMV020670	4.9 (±0.8)	1.1 (±0.2)	Malaria

C

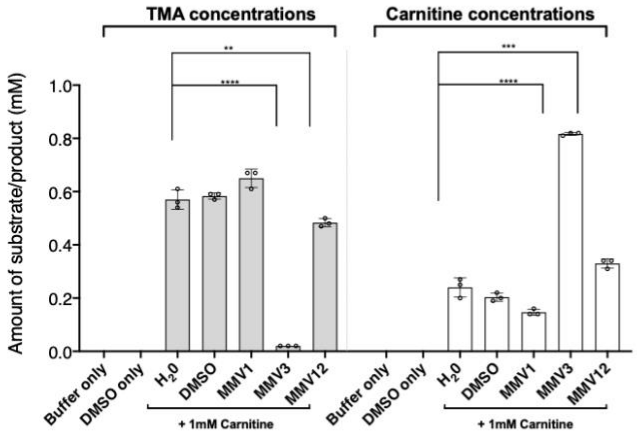

D

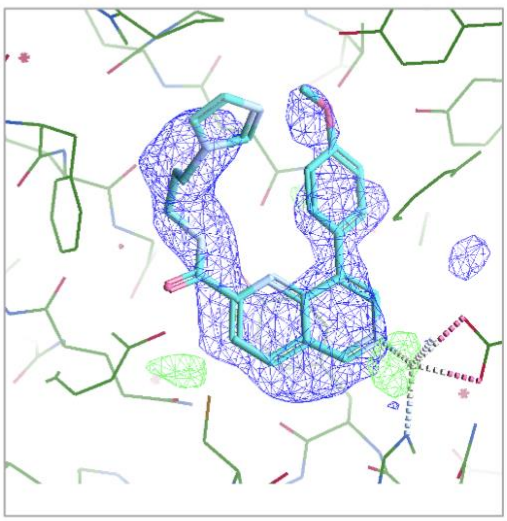

E

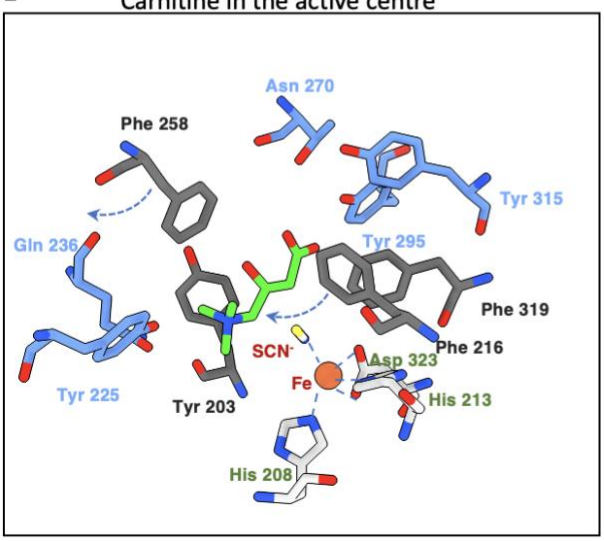

F

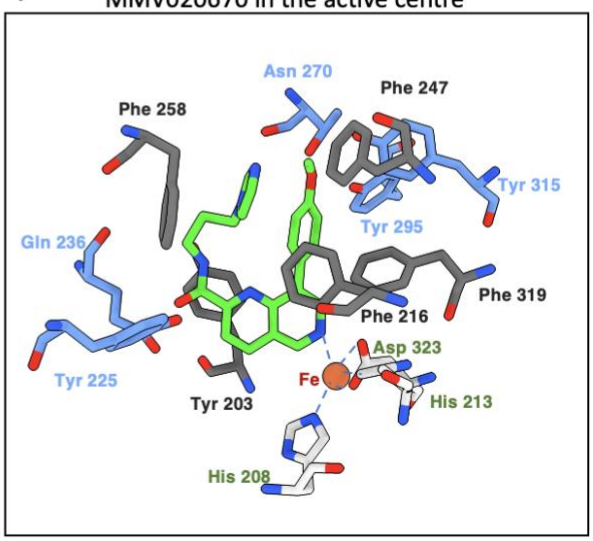

Figure 6 Structural basis of CntA inhibition

A, Chemical structures of the three CntA inhibitors : (MMV1) = MMV010764 (N-[(oxan-4-yl)methyl] - 5 - (thiophen - 2 - yl)imidazo[2,1 - b][1,3,4]thiadiazol - 2 - amine), (MMV3) =

MMV661713(6 - (5 - bromopyridin - 3 - yl) - N - [3 - (1H - imidazol - 1 - yl)propyl] - 2 - phenylpyrimidin - 4 - amine) and (MMV12) = MMV020670 (N - [3 - (1H - imidazol - 1 - yl)propyl] - 8 - methyl - 1,6 - naphthyridine - 2 - carboxamide).

B, A summary of the inhibitor assays with inhibitory IC_{50} data values shown for n = 3 replicates.

C, Evaluation of CntA protein inhibitors (MMV1, MMV3, MMV12) using *A. baumannii* bacterial cultures. Cells treated with inhibitors MMV3 ($p<0.0001$) and MMV12 ($p<0.001$) caused significant reduction in TMA formation from carnitine whereas MMV1 did not reduce TMA production. Carnitine was added to a final concentration of 1 mM prior to the incubations with/without additional inhibitors. Control runs of buffer only and DMSO only did not have carnitine in the treatment and no TMA was observed. N=3 for all conditions. Statistics was carried out using one-way ANOVA. **, $p<0.01$; ***, $p<0.001$; ****, $p<0.0001$.

D, A Polder OMIT map (Blue) of MMV12 (MMV020670) displayed at 3.0σ in the CntA active site.

E & F, A comparison of selected residues in the CntA active interacting with the carnitine substrate and MMV12 (MMV020670) inhibitor. Polar interacting residues (Magenta) remain unchanged whilst for the hydrophobic π-π interacting residues (Dark Grey), positional changes for Phe 258 and Phe 216 as indicated by dashed arrows in panel E.

Structural basis of carnitine monooxygenase CntA substrate specificity, inhibition and inter-subunit electron transfer

Mussa Quareshy, Muralidharan Shanmugam, Eleanor Townsend, Eleanor Jameson, Timothy D.H. Bugg, Alexander D Cameron and Yin Chen

J. Biol. Chem. published online November 6, 2020
